ZnO–MoS2-PMMA polymeric nanocomposites: A harmless material for water treatment

Maria Cantarella [a,1], Vanessa Spanò [a,2], Massimo Zimbone [a], Federico Giuffrida [a], Ernestino Lufrano [a], Vincenzina Strano [a], Giorgia Franzò [a], Gianfranco Sfuncia [b], Giuseppe Nicotra [b], Alessandra Alberti [b], Maria Antonietta Buccheri [a], Giancarlo Rappazzo [c], Elena Maria Scalisi [c], Roberta Pecoraro [c], Maria Violetta Brundo [c], Giuliana Impellizzeri [a,*]

[a] CNR-IMM, Via S. Sofia 64, 95123 Catania, Italy
[b] CNR-IMM, Zona Industriale, Strada VIII 5, 95121 Catania, Italy
[c] Department of Biological, Geological and Environmental Sciences, University of Catania, Via Androne 81, 95124 Catania, Italy

ARTICLE INFO

ABSTRACT

The realization of polymeric nanocomposites is a promising strategy for large-scale applications of photocatalytic nanomaterials, limiting their dispersion into the environment. In addition, in order to obtain very efficient materials, a valid solution can be the formation of heterojunctions that, reducing the electron-hole recombination phenomena, increases the performances of the photocatalysts. For this work, we have realized promising photocatalytic polymeric nanocomposites through the simple method of sonication and solution casting, using poly (methyl methacrylate) (PMMA) as supporting matrix, ZnO nanoparticles as photoactive material, and MoS_2 nanoflakes as co-catalyst for the realization of the heterojunction. Materials with several quantities of MoS_2 have been synthetized and characterized by scanning electron microscopy (SEM), contact angle measurements, X-ray diffraction analysis (XRD), UV–Vis spectroscopy, transmission electron microscopy (TEM), and photo-luminescence (PL). The photocatalytic performances of the obtained materials were evaluated by the photo-degradation under UV light irradiation of two different common pollutants: rhodamine B (RhB) and sodium dodecyl sulfate (SDS). The mechanism of the involved photocatalytic process was studied by the investigation of the main oxidants responsible of the photodegradation, using hole or radical scavengers. The antibacterial properties were investigated using *Escherichia coli* as a model organism. The eventual toxic effects of the prepared materials were studied on *Artemia salina*.

1. Introduction

Water quality is one of the main challenges that society will face during the next years. The industrial/agriculture discharge and other human activities release several kinds of chemicals into the environment, contaminating the available water resources. These chemicals belong to different categories, such as pesticides, dyes, pharmaceuticals, personal care products and their transformation products [1]. Most of these organic compounds are toxic and scarcely biodegradable, and often the conventional water treatment technologies are not able to remove them in a satisfactory way, or they are time and energy consuming. Hence, the development of new and efficient methods for water treatment is highly demanded [2–6].

Advanced oxidation processes (AOPs) are today considered effective methods for the destruction of recalcitrant organic pollutants of water [7]. AOPs depend on in-situ generation of reactive radicals capable of degrading organic molecules, by using light, chemicals, or other forms of energy. Among AOPs, heterogeneous photocatalysis has received a great attention within the scientific community, thanks to its potential to mineralize a wide range of organic contaminants at ambient temperature and pressure into harmless compounds [8,9]. This process employs inorganic semiconductors that act as photocatalysts; when they are

irradiated with photons of energies greater than their band-gap energies the formation of electron-hole pairs occurs [8,9]. The photo-generated holes oxidize the water molecules producing the hydroxyl radicals, meanwhile the photo-excited electrons reduce the oxygen molecules generating the superoxide radical anions [8,9]. These radicals, but also the holes, are the main responsibles of the degradation processes [8,9].

Among the several studied semiconductors, zinc oxide (ZnO) has emerged as a valid candidate for photocatalytic applications, thanks to some intrinsic properties, such as high availability, low cost, large and direct band-gap in the UV region, suitable valence and conduction band edge potential with respect to the natural hydrogen electrode (NHE) used as reference [10,11].

Compared to bulk material, nanostructured ZnO possesses additional advantages for applications in photocatalysis. Indeed, the nanomaterials have a higher surface to volume ratio, allowing a more efficient photocatalysis. In addition, the synthesis of ZnO nanomaterials (nanoparticles, nanotubes, nanowires, nanocubes, nanonuts, nanofibers, etc.) is quite easy, increasing the motivation for the use of this material for photocatalytic applications [12–14].

However, a shortcoming limits the application of pure ZnO as photocatalyst, which is the high recombination rate of the electron-hole pairs, upon UV light irradiation, before they can reach the semiconductor surface [15]. Many strategies have been studied to increase the electron-hole separation, such as the combination of the photocatalyst with other semiconductors [16], carbon materials [17], or noble metals [18,19]. These co-catalysts not only extract the charges but can also serve as active sites for molecules reduction or oxidation.

A valid co-catalyst is represented by molybdenum disulfide (MoS_2). This is a two-dimensional (2D) layered material composed by Mo atoms sandwiched between two layers of hexagonally close-packed S atoms. A monolayer of MoS_2 has a direct band-gap of about 1.8–1.9 eV; by increasing the number of stacking layers, the band-gap decreases down to an indirect band-gap of about 1.0–1.2 eV for the bulk material [20]. Thanks to these characteristics, MoS_2 is used in combination with large band-gap semiconductors, such as ZnO [21–24]. With this configuration, a heterojunction is formed at the interface region; electrons and holes can migrate between the semiconductors, enhancing their spatial separation and consequently increasing the photocatalytic efficiency of the ZnO [25,26].

An important aspect to be considered concerns the dispersion of the photocatalytic nanomaterials into the environment after the water purification process. The impact of nanomaterials on human health and on ecosystem is still a matter of debate, and for this reason a carefully recovery is needed [27]. However, due to the low dimension of the nanomaterials, the feasible methods for their gathering are energy and time consuming, and this is indeed the most important limitation for their application on a large scale. For this reason, their immobilization in a suitable support appears the winning strategy for their use. Polymers are considered the most promising hosting matrices for the realization of hybrid nanocomposite materials because of their ease of production, low cost, light weight, and ductile nature. By combining the attractive functionalities of both components (i.e. the organic and inorganic one), nanocomposites derived from organic polymers and inorganic nanomaterials display excellent properties, thus deserving applications in many fields [28–31].

In this work we have used poly (methyl methacrylate) (PMMA) as supporting matrix, due to its transparency to visible light and resistance to UV irradiation [32]. Through the simple method of sonication and solution casting we have realized photocatalytic nanocomposites composed of PMMA and ZnO nanoparticles coupled with MoS_2 nanoflakes, to take the advantages of the formation of heterojunctions in terms of increasing of the photocatalytic efficiency. To our knowledge, this is the first time that polymeric nanocomposites realized with PMMA, ZnO, and MoS_2 were produced and studied for photocatalytic applications.

2. Experimental

2.1. Preparation methods

The photocatalytic polymeric nanocomposites studied in this work were realized by the simple method of sonication and solution casting [32,33].

All the materials used in this work (i.e. PMMA, ZnO, MoS_2 and solvent) were purchased from Merck and used as-received without any further purification. The ZnO-MoS_2-PMMA composites were prepared as follow: in a vial, indicated with A, 800 mg of PMMA powders (molecular weight ~ 120000) were dissolved in 4 mL of acetone; in a separate vial, indicated with B, 40 mg (corresponding to 5 wt% respect to the polymeric amount) of ZnO nanoparticles (<100 nm particle size), and an appropriate quantity of MoS_2 nanoflakes (nominal size of 90 nm) were dispersed in 4 mL of acetone and sonicated for 45 min. In detail, we prepared three different typologies of samples corresponding to three different weight percentages of MoS_2 nanoflakes (10 wt %, 20 wt %, 30 wt %) respect to the used ZnO. After the sonication, for each sample, the dispersion in vial B was mixed with the polymeric solution in vial A and sonicated again for 1 h. After that, the resulting mixtures were cast into glass Petri dishes (6 cm in diameter), and they were maintained overnight at 4 °C to allow the evaporation of the solvent and to produce the nanocomposite films. After this time, the prepared films were peeled off from the Petri dish, obtaining freestanding films.

Pure PMMA films and ZnO-PMMA films, used as references, were prepared with the same procedure. Several films of the different typologies were produced.

Hereafter, the samples will be simply called: "PMMA", "ZnO-PMMA", "ZnO-10 % MoS_2-PMMA", "ZnO-20 % MoS_2-PMMA", "ZnO-30 % MoS_2-PMMA".

The tested samples' surface was the back surface, i.e. the surface in contact with the Petri dish during the evaporation of the solvent, because it resulted richer in nanopowders, due to their sedimentation, as observed in our previous work [32].

2.2. Characterizations

The morphology of the polymeric nanocomposites was investigated by scanning electron microscopy (SEM), using a field emission Zeiss Supra 25 microscope operating at 3 kV. The investigated samples were previously coated, by sputter deposition, with a 5 nm-film of gold to reduce the electron beam charging of the insulating polymer.

The surface wettability of the realized samples was characterized by measuring the contact angles using a DATAPHYSICS-OCA 15 PRO device. The liquid used was deionized water. The mean value of three measurements, in three different areas of each sample, was recorded.

X-ray diffraction (XRD) analyses were done using a Rigaku Smartlab diffractometer equipped with a rotating anode operating at 45 kV-100 mA, and with a HyPix 3000 detector.

UV–Vis total reflectance spectra were acquired using a PerkinElmer Lambda 1050+ UV/Vis/NIR spectrometer equipped with a 100 mm integrating sphere in the range between 250 and 950 nm.

Transmission electron microscopy (TEM) characterization was preceded by a careful preparation of the materials. The samples were cut in stripes (lateral dimension <1 mm) and embedded in resin using the Poly/Bed® 812 (Luft formulations) embedding kit/DMP-30. The resin blocks were then trimmed with a Leica EM TXP to produce a flat block face centered on the ZnO-MoS_2-PMMA composite. Finally, 100 nm thin sections were cut using a Leica EM UC7 ultramicrotome equipped with a Diatome ultra 35° diamond knife and collected on copper TEM grids. TEM analyses were performed using a Jeol ARM-200F transmission electron microscope operating in scanning mode (S/TEM) at an acceleration voltage of 200 kV, equipped with a cold field emission gun, a CEOS CESCOR spherical aberration corrector, and a Gatan Imaging filter (GIF) QuantumER for dual Electon Energy Loss Spectroscopy (EELS).

Spectrum Imaging (SI) mode, which combines STEM imaging and EELS spectroscopy, was used to obtain spatially resolved chemical information.

Photoluminescence (PL) measurements were performed at room temperature by exciting the samples with the 325 nm line of a continuous HeCd laser chopped through an acousto-optic modulator at a frequency of 55 Hz. The PL signals were analyzed through a single grating monochromator, detected with a visible photomultiplier and recorded with a lock-in amplifier having the acousto-optic modulator frequency as a reference.

2.3. Photocatalytic tests

The photocatalytic activity of the obtained materials was evaluated by the degradation of rhodamine B (RhB), a common textile dye today considered a water contaminant. At the beginning of each experiment, 1 cm^2 of sample to be tested was immersed in 2 mL of dye aqueous solution (1.5×10^{-5} M) in a cylindrical reactor (with a diameter of 1.5 cm) and left in the dark to allow the physical adsorption reaches the equilibrium. The latter was verified by picking up all the 2 mL of the solution and measuring the variation in the dye concentration spectrophotometrically, using a Lambda 45 PerkinElmer spectrophotometer, through the absorbance peak at 554 nm. Indeed, in the Lambert-Beer regime, the absorbance of the solution is proportional to the dye concentration. Then, the solution was put back into the reactor. Once the saturation was reached (usually after 60 min), the reactor was covered with a quartz glass, to avoid the evaporation of the solution, and irradiated by an UWAVE LED UV lamp system, with an emission centered at 365 nm (full width at half maximum, FWHM, of 10 nm) and an irradiance of 10 mW/cm^2. The RhB degradation was measured spectrophotometrically at regular time intervals (every 30 min) for 240 min, picking up every time all the 2 mL of the solution to be analyzed and putting back the analyzed solution into the cylindrical reactor, containing the corresponding sample, after the measurement. As control, the RhB photodegradation without any sample in the solution was monitored in all the experiments.

The stability of the nanocomposites was checked by repeating four times the RhB degradation test, by using the same fragment of every sample. Before each cycle, the samples were rinsed in deionized water, arranged in clean and empty cylindrical vessels and UV-irradiated in dry conditions for 60 min. Then, the aqueous solution of RhB was put in contact with the samples and the photocatalytic tests were performed as described before.

The photocatalytic properties of the samples were also tested by the degradation of sodium dodecyl sulfate (SDS), an anionic surfactant used in many cleaning and hygiene products that makes it one of the major grey-water contaminants. SDS degradation was monitored, after 4 h of UV light irradiation, using a Hach DR 3900 spectrophotometer and the related LCK 432 cuvette kits. The starting concentration of SDS was 1.5×10^{-5} M, and also in this case the SDS degradation without any sample was verified as a control experiment. The experimental set-up was the same to the one described for the tests with RhB.

In order to study the mechanism involved in this photocatalytic degradation, the detection of the main oxidant was performed by using disodium ethylenediamine tetraacetate (EDTA-2Na), as holes scavenger, or *tert*-butyl alcohol (*t*BuOH), as radicals scavenger (i.e. oxygenous radicals) [34,35]. In detail, the degradation of RhB was carried out with the procedure described above but adding EDTA-2Na or *t*BuOH, both 10^{-3} M, during the photocatalytic test.

The estimated experimental error for the photocatalytic tests was 5 %.

2.4. Antibacterial tests

Antibacterial activity was tested on *Escherichia coli* (*E. coli*) ATCC8739 strain. Bacteria were routinely maintained through

spreading on McConkey agar plates. To run the experiments, a single colony was picked, inoculated in 30 mL of Luria-Bertani (LB) broth, and let grown overnight at 37 °C in aerobic conditions under constant agitation at 180 revolutions per minute (rpm). The following morning, bacterial growth was checked through optical density measures at 600 nm. Bacteria were diluted up to 106 colony forming units per mL (CFU/mL) in phosphate saline buffer (PBS). According to the ISO standard 27447:2019 [36], a humid chamber was realized, and samples were protected by a quartz glass to avoid drying during irradiation. A volume of 100 μL of the 106 CFU/mL bacterial solution was spread onto the samples and a cover glass of the same dimensions was put on top to flatten the solution out, thus favoring the contact between the bacteria and the tested surface. An UV lamp, centered at 368 nm, with a FWHM of ∼10 nm, and with an irradiance of 1.1 mW/cm^2 was used to promote the photocatalysis. Bacteria not exposed to UV light nor to any nanocomposites, as well as a sample exposed to PMMA and UV only, were run in parallel as controls. After 1 h exposure, bacteria were recovered, conveniently diluted and plated in LB Agar Petri dishes that were incubated at 37 °C. Colonies were counted the following day. Bacterial survival was normalized toward the untreated sample and plotted as percentage. Experimental error was around 5 %. Experiments were made in triplicates.

2.5. Ecotoxicology tests

Artemia salina dehydrated cysts are commercially available (Artemio Pur® JBL GmBh&Co., Germany) then they were purchased from a local aquarium. They were placed in a beaker containing ASPM artificial sea water (35 g in 1 L of deionized water under stirring) to select the sink cysts and discard those that floating. All cysts collected (1 g) were incubated in ASPM water (NaCl 26.4 g/L, KCl 0.84 g/L, CaCl$_2$·H$_2$O 1.67 g/L, MgCl$_2$·6H$_2$O 4.6 g/L, MgSO$_4$·7H$_2$O 5.58 g/L, NaHCO$_3$ 0.17 g/L, H$_3$BO$_3$ 0.03 g/L in MilliQ water) [37,38]. They were left under conditions of gentle aeration and continuous illuminations at room temperature (28–30 °C), and within 36–48 h they hatched. Subsequently, nauplii at stage II and III were selected and transferred using a micropipette to 50 mL glass beakers. We set up 3 beakers: two for exposed groups (ZnO-PMMA and ZnO-30 % MoS$_2$-PMMA), and one for the unexposed group (i.e., the control). Both types of nanomaterials were placed inside the beakers, each one filled with 10 mL of ASPM water; a number of 30 nauplii were placed in all beakers as in the exposed groups as in the control ones. Control nauplii were exposed only to ASPM water. The incubation period was 24/48 h at 26 °C, to evaluate the endpoint of immobility, i.e. death. Using a stereomicroscope the number of surviving and dead nauplii were counted at 24 h and 48 h. The death % of the nauplii for each group was calculated as follow: (n. Dead nauplii/n. Total animal treated) × 100. A nauplium is considered dead when it does not move its antennae and remain immobile for at least 10 continuous seconds of observation even if there is a slight agitation of the water. At the end of the test, for each group nauplii were collected randomly. They were sacrificed and fixed with formalin at 4 % (Bio-Optica); the development and any morphological alterations of nauplii were evaluated through an optical microscope (Set E200 Nikon) equipped with a camera (CMOS Nikon). Images were acquired for all the groups (both exposed and control), therefore any malformations or growth alteration of the exposed nauplii were compared to control.

3. Results and discussion

The morphological characterization of the nanocomposites was performed by SEM analyses. Fig. 1 reports a SEM in plan-view of the reference material, i.e. ZnO-PMMA (Fig. 1a), and of the sample with 30 $_{wt}$% of MoS$_2$, ZnO-30 % MoS$_2$-PMMA (Fig. 1b). The first image clearly shows the ZnO nanoparticles emerging from the polymeric surface, while in the second one it is possible to distinguish the presence of MoS$_2$ nanoflakes, as expected, with the evidence of nanoparticles aggregation.
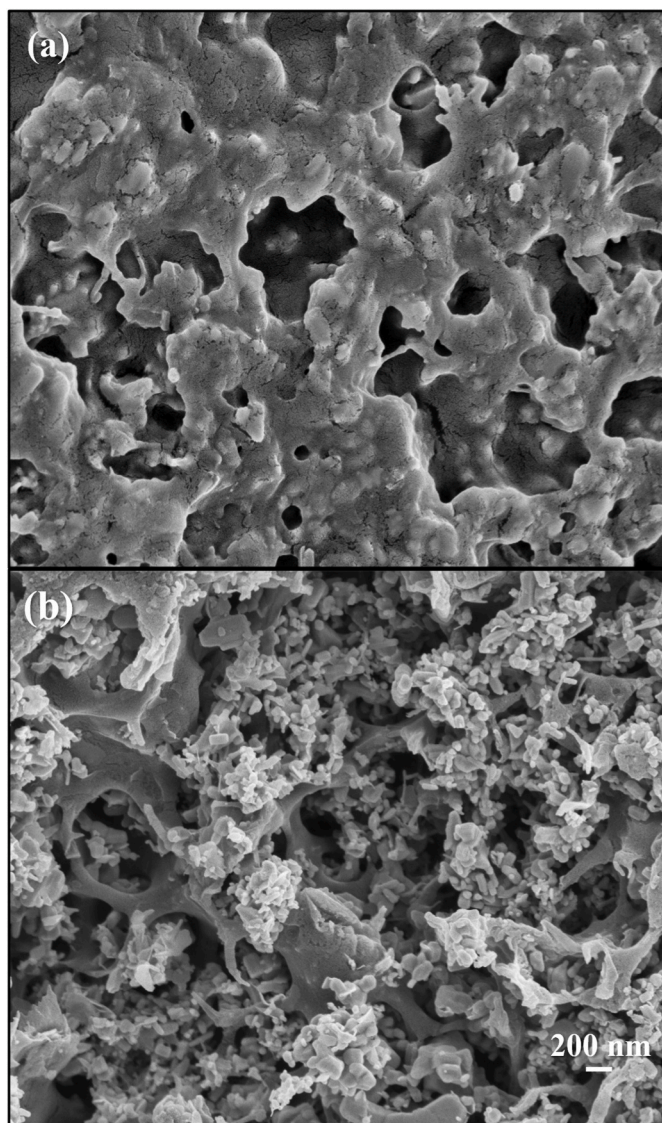
Fig. 1. Plan-view SEM images of (a) ZnO-PMMA and (b) ZnO-30 % MoS$_2$-PMMA composites. The scale bar in (b) refers to both images.

The size of ZnO and MoS$_2$ nanopowders seems to be in agreement with the nominal values provided by the manufacturer and reported in the Experimental section. In both plan views, the presence of superficial cavities ascribable to the solvent evaporation are visible.

Since the wettability of the surfaces influences their photocatalytic aptitude (affecting the initial adsorption of the pollutants on the sample surface), the contact angle of each sample typology was estimated. Table 1 reports the mean values of contact angles measured on the surfaces of the samples with different quantity of MoS$_2$ nanoflakes and of the reference material. It is worth noting that the presence of MoS$_2$ did not influenced the wettability of the surfaces; the contact angle values

Table 1
Contact angle values for all the investigated samples: ZnO-PMMA, ZnO-10 % MoS$_2$-PMMA, ZnO-20 % MoS$_2$-PMMA, ZnO-30 % MoS$_2$-PMMA.

Sample	Contact angle (°)
ZnO-PMMA	68.9 ± 6.9
ZnO-10 % MoS$_2$-PMMA	86.8 ± 8.7
ZnO-20 % MoS$_2$-PMMA	70.0 ± 7.0
ZnO-30 % MoS$_2$-PMMA	73.6 ± 7.4

are indeed comparable within the experimental errors for all the samples. In addition, considering the contact angle values, all the samples showed a hydrophilic nature [39].

Fig. 2 compares the diffraction patterns of the two samples made of ZnO-PMMA and ZnO-30 % MoS$_2$-PMMA. In the first case (blue line in Fig. 2), ZnO peaks arise from a zincite structure with lattice parameters a = 0.326 nm, b = 0.326 nm, c = 0.522 nm. In the second case (magenta line in Fig. 2), a blend of materials is detected. In addition to ZnO contributions, peaks associated to hexagonal MoS$_2$ were detected with lattice parameters a = 0.316 nm, b = 0.316 nm, c = 1.231 nm. In this sample, we also noticed a slight change of the lattice parameters in the ZnO structure, with a = 0.325 nm, b = 0.325 nm, c = 0.521 nm. This slight contraction of the unit cell (DV/V = −0.8 %), ascribed to strains due to the presence of MoS$_2$, caused a rightwards shift of all peaks with respect to what detected in the ZnO-PMMA sample.

Fig. 3a shows the diffuse reflectance spectra of ZnO-PMMA and ZnO-30 % MoS$_2$-PMMA samples. The sharp increases in the reflectance of ZnO-PMMA sample at about 400 nm indicates the ZnO adsorption edge, while the weak and smooth decrease of the signal for wavelengths higher than 450 nm is related to the light scattering phenomena of the agglomerated ZnO nanoparticles. The band-gap energy of ZnO was estimated by using the procedure reported in ref. [40], applying the Kubelka-Munk and Tauc plot approaches. Indeed, in Fig. 3b, we reported the $(F(R)h\nu)^{1/2}$ as a function of the photon energy from which it was possible to estimate an optical band-gap of (3.19 ± 0.16) eV for the ZnO-PMMA sample. This result is in agreement with the values reported in the literature for ZnO [41–43]. In Fig. 3a, the spectra of the ZnO-30 % MoS$_2$-PMMA sample was also reported. The small but sharp increase of the reflectance at about 400 nm is related to the ZnO absorption feature. The estimated optical band-gap (Fig. 3b) was (3.22 ± 0.16) eV, that is equal within the experimental error to the band-gap estimated for the ZnO-PMMA sample. In the region between 1.7 and 2 eV of Fig. 3b, the curve of ZnO-30 % MoS$_2$-PMMA shows a linear increase with the energy that is associated to the band-gap of MoS$_2$. The procedure reported in ref. [40] allowed us to estimate a band-gap of (1.68 ± 0.08) eV. This value is compatible with the presence of a mixture of mono and multi-layer MoS$_2$ nanoflakes [20].
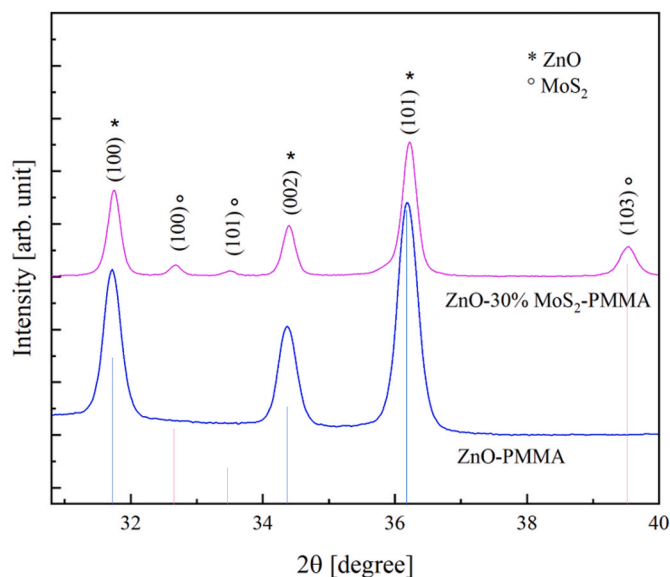

Fig. 2. XRD patterns of ZnO-PMMA (blue line below) and ZnO-30 % MoS$_2$-PMMA (magenta line above). The diffraction peaks of the two inorganic nanomaterials are explicitly indicated. Reference patterns are taken from MoS$_2$ (JPC2.2CA:00-037-1492) with hexagonal lattice structure and Space group 194 (P63 mmc); ZnO (JPC2.2CA:01-070-2551) with hexagonal lattice structure and Space group 186 (*P*63mc). The lattice parameters are reported in the main text.
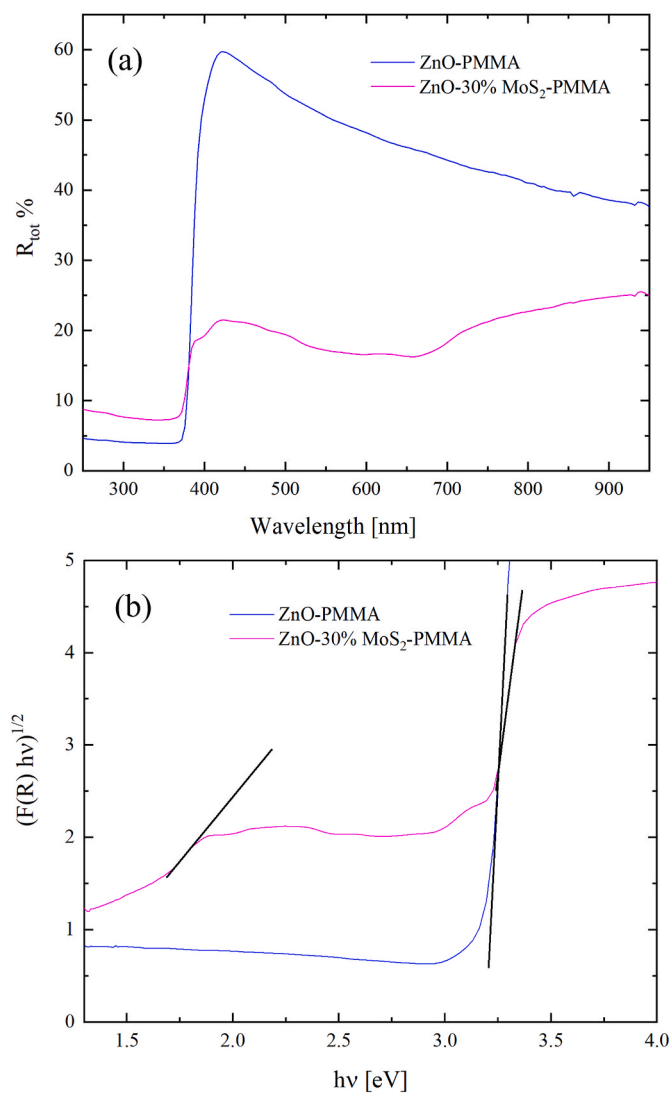
Fig. 4a presents a high-angle annular dark field (HAADF) STEM image of the composite film showing both ZnO nanoparticles and MoS$_2$ nanoflakes. ZnO nanoparticles possess regular and faceted shape because of their close-packed crystal structure with size in the 50–100 nm range. MoS$_2$ nanoflakes exhibited elongated shape with wrinkled structure, with typical lateral size in the 100–500 nm range. The HAADF STEM analysis highlighted the close contact between ZnO nanoparticles and MoS$_2$ nanoflakes, which is pivotal for the improved photocatalytic activity.

Fig. 4b reports the chemical analysis obtained by SI-EELS. Chemical maps of single elements are reconstructed using Zn L-edge at 1020 eV, Mo M-edge at 227 eV, O K-edge at 532 eV, and S L-edge at 165 eV. These maps showed an exact correspondence between Zn and O and between Mo and S signals, allowing to clearly distinguish ZnO nanoparticles from MoS$_2$ nanoflakes, also confirming their intermixing at the nanoscale, as evidenced by the aggregated colour map reported in Fig. 4c.

In Fig. 5 the PL spectra measured at room temperature for a ZnO-PMMA sample and for the samples having also different concentrations of MoS$_2$ nanoflakes are reported. A detail of the PL spectra limited to the visible part of the spectra is reported in the inset. The PL spectrum of the ZnO-PMMA sample (black line) consists of two peaks, one in the
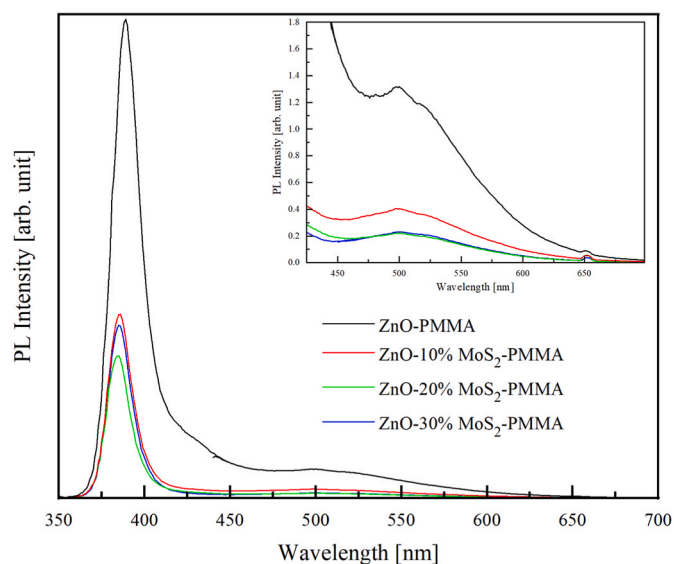
Fig. 3. Total reflectance spectra (a), and Tauc plot of the Kubelka-Munk function (b) of ZnO-PMMA (blue line) and ZnO-30 % MoS$_2$-PMMA (magenta line) samples.

Fig. 5. PL spectra of ZnO-PMMA (black line), ZnO-10 % MoS$_2$-PMMA (red line), ZnO-20 % MoS$_2$-PMMA (green line), ZnO-30 % MoS$_2$-PMMA (blue line).
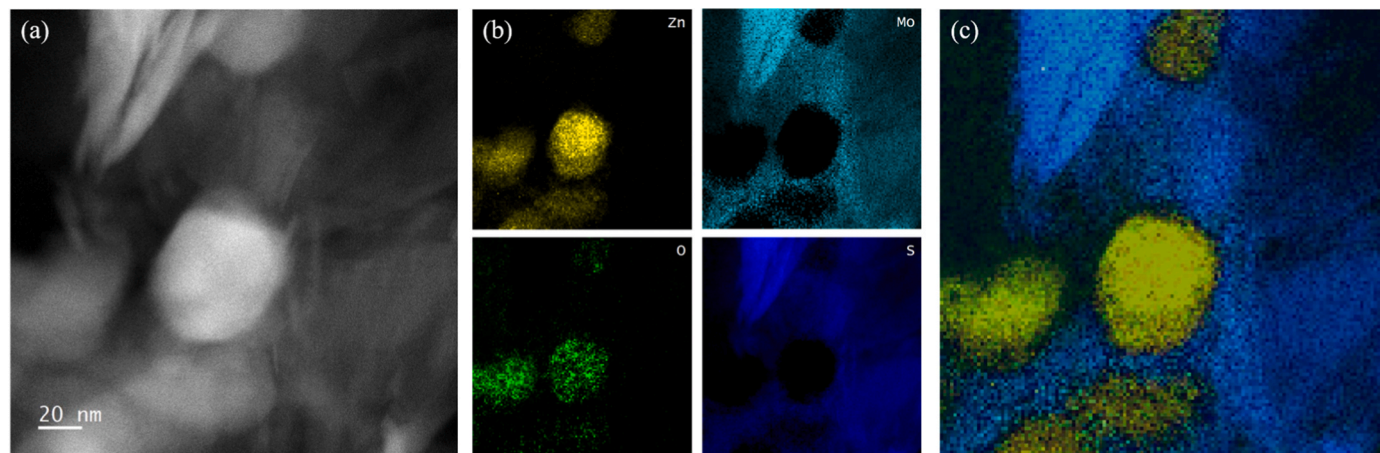

Fig. 4. HAADF STEM image of the ZnO-30 % MoS$_2$-PMMA composite film (a); Zn (yellow), Mo (cyan), O (green) and S (blue) chemical maps obtained from the corresponding EELS signals in SI mode (b); aggregated chemical map showing ZnO nanoparticles and MoS$_2$ nanoflakes (c).

UV (at 388 nm) and one at around 500 nm and both peaks can be attributed to an electron-hole recombination in the ZnO nanoparticles [44]. In particular, the UV peak is associated to a band-to-band recombination in the ZnO nanostructures, while the visible peak is due to defect bands [41,44]. When MoS_2 nanoflakes are added at a concentration of 10 % (red line), the shape of the PL spectrum is not modified but the intensity of both the UV and visible peaks decreases by almost a factor of 3. A further increase in the MoS_2 nanoflakes concentration produces only a slight further decrease of the PL emission, without any change in the shape of the spectra or the appearance of any further emission lines assignable to MoS_2. Therefore, in the presence of MoS_2 radiative recombination phenomena are drastically reduced, as testified by the reduction of UV emission, due to the charge separation in the heterojunction between ZnO and MoS_2.

The photocatalytic activity of all the prepared nanocomposites (ZnO-PMMA, ZnO-10 % MoS_2-PMMA, ZnO-20 % MoS_2-PMMA, ZnO-30 % MoS_2-PMMA), 1 cm^2 in size, was evaluated by the degradation of RhB, monitoring spectrophotometrically the absorption peak at 554 nm. Fig. 6 reports the variation in the dye concentration, proportional to the absorbance (Lambert-Beer law), as a function of the irradiation time. The grey zone in the graph represents the initial step of preconditioning led in the dark, which allows the physical adsorption to reach the equilibrium. This saturation level was reached within 60 min for all the tested samples. The white area in the graph represents, instead, the variation in the RhB concentration under UV light irradiation. All the nanocomposites showed a remarkable photocatalytic efficiency. The best performance was obtained with the sample containing the highest quantity of MoS_2 (i.e., ZnO-30 % MoS_2-PMMA), that was able to degrade in 4 h of illumination ~75 % of the dye (down triangles), while the reference material (i.e., ZnO-PMMA) in the same time frame degraded ~55 % of the RhB (squares). The other two samples (i.e., ZnO-10 % MoS_2-PMMA and ZnO-20 % MoS_2-PMMA) showed an intermediate efficiency between the samples mentioned before. Thus, it is possible to highlight an increase in the efficiency proportional to the quantity of MoS_2.

The photodegradation reaction rates [9] of RhB by the different investigated samples are reported in Table 2. In particular, the estimated kinetic constant resulted $(2.41 \pm 0.12) \times 10^{-3}$ min^{-1} for the best performer (i.e., ZnO-30 % MoS_2-PMMA), versus $(1.59 \pm 0.08) \times 10^{-3}$ min^{-1} for the reference material (i.e., ZnO-PMMA).
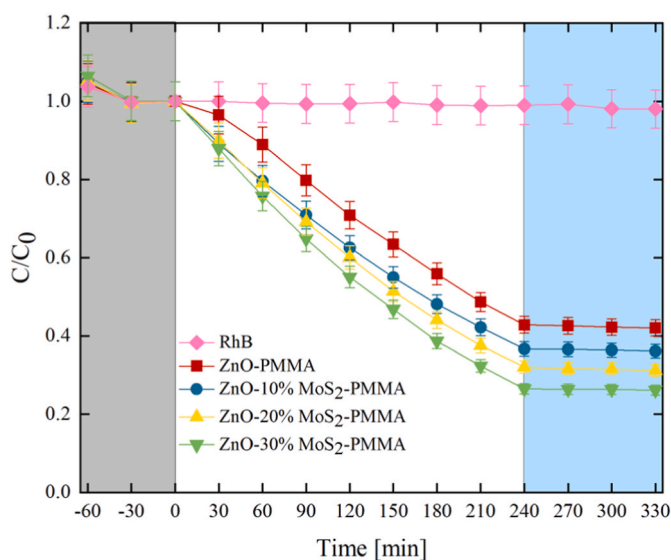
Table 2
Kinetic constants of the photocatalytic degradation of RdB by the polymeric nanocomposites with different quantity of MoS_2 nanopowders (0, 10, 20, 30 %).

Sample	Rate costant (min^{-1})
ZnO-PMMA	$(1.59 \pm 0.08) \times 10^{-3}$
ZnO-10 % MoS_2-PMMA	$(1.81 \pm 0.09) \times 10^{-3}$
ZnO-20 % MoS_2-PMMA	$(2.08 \pm 0.10) \times 10^{-3}$
ZnO-30 % MoS_2-PMMA	$(2.41 \pm 0.12) \times 10^{-3}$

In order to investigate an eventual release of nanomaterials from the polymeric matrix during the photocatalytic process, the following test was performed. The samples were removed from the solutions after 240 min of irradiation and the irradiation with the UV-lamp was maintained for further 90 min. No reduction of RhB was observed (light-blue area in the graph), so indicating that not enough nanomaterials were released that would lead a detectable photodegradation.

The discoloration of pure RhB, without any photocatalyst, was also performed as a control (diamonds), and no variation was observed, as expected.

To evaluate the stability of the investigated materials, we re-used the same fragment of each sample for the degradation of RhB and checked the photocatalytic efficiency for several cycles. The results are summarized in Fig. 7. We found that the photocatalytic efficiency does not significantly change after four cycles, suggesting that such nanocomposites can be efficiently reused for repeated cycles.

With the aim of confirming the photocatalytic efficiencies obtained by the degradation of RhB and to test the capacity of our samples in degrading other organic pollutants, the photocatalytic degradation of SDS was studied. The obtained results were reported in Fig. 8. The figure shows the percentage of removed SDS after 4 h of UV light irradiation for all the investigated samples. Also with this pollutant the best performance was obtained by the sample with 30 % of MoS_2, that was able to degrade ~75 % of the organic compound. On the contrary, without the presence of MoS_2 the sample ZnO-PMMA degrades just under 20 % of SDS. The observed low efficiency in the degradation of SDS with respect of RhB is probably due to the recalcitrant nature of the SDS [45]. It is possible to note, again, an increase of the efficiency with the MoS_2 quantity.

Table 3 reports the photodegradation reaction rates of SDS by the different investigated samples. The kinetic constant resulted $(2.32 \pm$
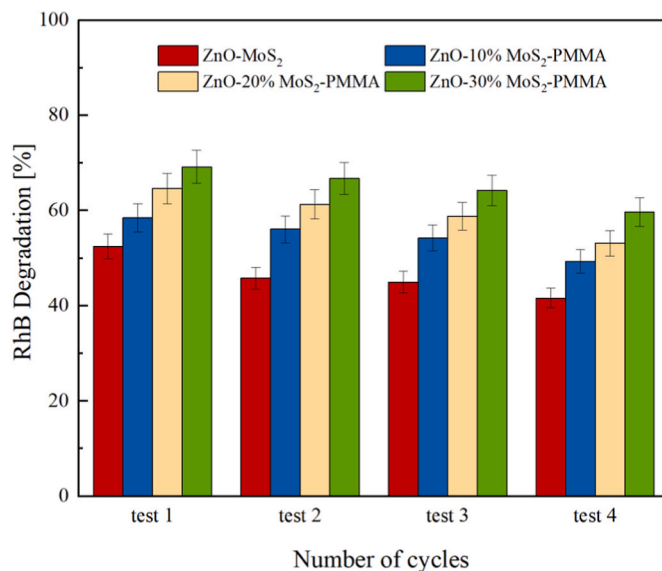

Fig. 6. Degradation of RhB by: ZnO-PMMA (squares), ZnO-10 % MoS_2-PMMA (circles), ZnO-20 % MoS_2-PMMA (up triangles), ZnO-30 % MoS_2-PMMA (down triangles), and pure RhB as control (diamonds). Grey area: test in the dark; white area: test under UV light; light blue area: test without photocatalysts.

Fig. 7. Recyclability of ZnO-PMMA, ZnO-10 % MoS_2-PMMA, ZnO-20 % MoS_2-PMMA, and ZnO-30 % MoS_2-PMMA after four tests of RhB photodegradation.
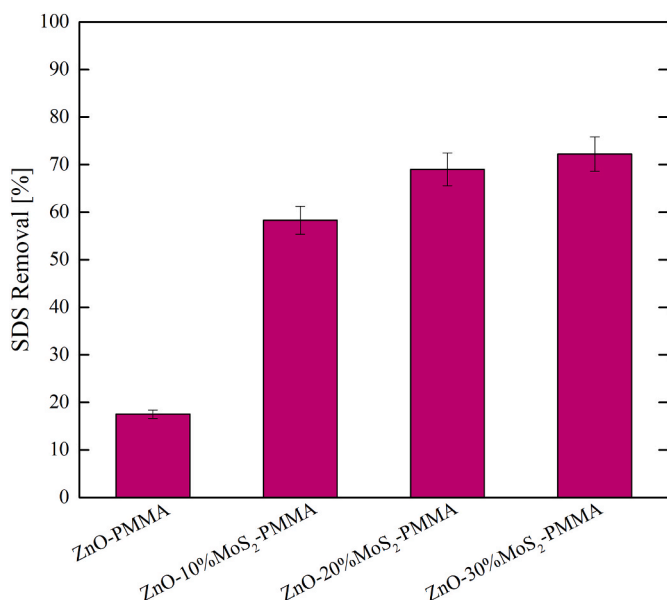
Fig. 8. Degradation of SDS after 4 h under UV light irradiation in the presence of ZnO-PMMA, ZnO-10 % MoS$_2$-PMMA, ZnO-20 % MoS$_2$-PMMA, ZnO-30 % MoS$_2$-PMMA.

Table 3
Kinetic constants of the photocatalytic degradation of SDS by the polymeric nanocomposites with different quantity of MoS$_2$ nano-powders (0, 10, 20, 30 %).

Sample	Rate costant (min^{-1})
ZnO-PMMA	$(0.34 \pm 0.02) \times 10^{-3}$
ZnO-10 % MoS$_2$-PMMA	$(1.58 \pm 0.08) \times 10^{-3}$
ZnO-20 % MoS$_2$-PMMA	$(2.12 \pm 0.11) \times 10^{-3}$
ZnO-30 % MoS$_2$-PMMA	$(2.32 \pm 0.12) \times 10^{-3}$

0.12) $\times 10^{-3}$ min^{-1} for the ZnO-30 % MoS$_2$-PMMA samples, versus (0.34 $\pm$ 0.02) $\times 10^{-3}$ min^{-1} for the ZnO-PMMA sample, with an increment of a factor of $\sim$7. It worth to note that the effect of the presence of MoS$_2$ is now more evident than in the case of RhB, maybe due to the recalcitrant nature of the SDS [45].

Photocatalytic tests were also performed under visible light, using a solar simulator Verasol-2 ORIEL LSS-7120 (400–1100 nm, irradiance: 1 kW/m^2); no activity was revealed because the small band-gap of MoS$_2$ induces a fast recombination rate of the photo-generated charge carriers. Moreover, it is known that the valence band edge potentials for bulk MoS$_2$ and monolayer MoS$_2$ were estimated to be 1.40 eV and 1.78 eV, respectively, which are not oxidative enough to generate free radicals for the decomposition of pollutants [46].

The knowledge of the main oxidant responsible of the photocatalytic process is important to know the mechanism involved during the photodegradation process, namely if it is due to photo-generated holes directly or it is mediated by oxygenous radicals. This investigation can be performed through radicals and holes trapping experiments. For this purpose, in this work, we used EDTA-2Na as holes scavenger and *t*BuOH as radicals scavenger, during the photodegradation of RhB [34]. In particular, we prepared two different solutions of RhB, in one of these solutions we added the needed amount of EDTA-2Na to obtain a concentration of 10^{-3} M, in the other one we added the needed amount of *t*BuOH to obtain a concentration of 10^{-3} M, too. Then, with the as-prepared solutions, the photocatalytic tests were performed with the same procedure described in the Experimental section, and compared with the results obtained with a solution of pure RhB. The obtained results are summarized in Fig. 9, in which we reported the kinetic constant for the degradation reaction of RhB by using ZnO-PMMA
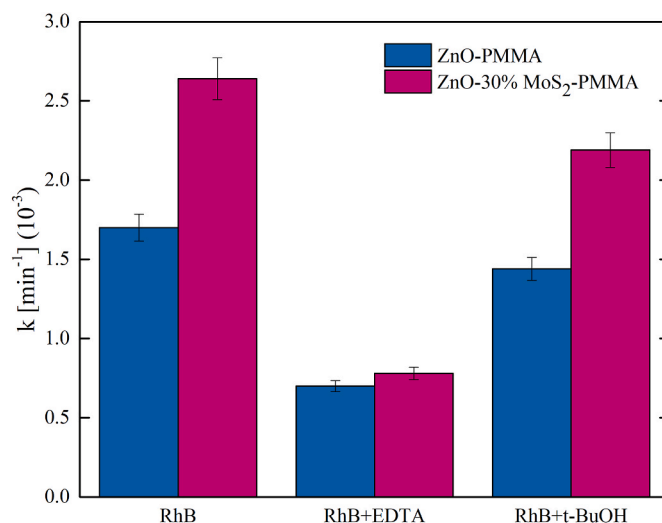

Fig. 9. Photodegradation of RhB by ZnO-PMMA and ZnO-30 % MoS$_2$-PMMA immersed in a solution of pure RhB or adding EDTA-2Na (hole scavenger) or *t*BuOH (radical scavenger).

sample or the most efficient one, i.e. ZnO-30 % MoS$_2$-PMMA, immersed in a solution of pure RhB, or in a RhB solution containing the hole scavenger or in a RhB solution containing the radical scavenger. In addition, for an easier understanding of the results, in Table 4 the photodegradation reaction rates of RhB in the different experimental conditions are reported. It is worth to note that, for all the solutions, the pH was measured before each experiment and in each solution it was around 7.5, independently from the presence of the scavenger. For both materials, the photodegradation process was decelerated whether in the presence of EDTA-2Na or *t*BuOH. However, a higher decrease was observed with the EDTA-2Na, so indicating that the photo-generated holes were the main oxidant involved in the photodegradation of the pollutant. Hence, the photodegradation caused by the holes was the dominant process for the prepared materials.

Antibacterial properties were studied using *Escherichia coli* as a model organism, a well-known Gram-negative bacterium considered as an indicator of water fecal contamination. The ATCC8739 strain, chosen for this experimental set up, is not a genetically modified strain for molecular biology purposes, and it is used for a number of quality control applications. Among nanocomposites containing MoS$_2$, possible antibacterial activity was explored for the ZnO-30 % MoS$_2$-PMMA sample, which is the one showing best photocatalytic activity, as described before. PMMA and ZnO-PMMA samples were used as references. After 1 h of exposure to the nanocomposites, bacteria survival was reduced up to $\sim$35 % by the ZnO-PMMA sample, while in the case of ZnO-30 % MoS$_2$-PMMA it was reduced up to $\sim$10 % (Fig. 10). In line with the results obtained by photocatalysis testing, the sample ZnO-30 % MoS$_2$-PMMA showed an increase in the antibacterial activity, if compared with nanocomposites containing only ZnO. Possibly, the effect of the enhanced photo-generated electron-holes separation, due to

Table 4
Kinetic constants of the photocatalytic degradation of RhB by ZnO-PMMA and ZnO-30 % MoS$_2$-PMMA immersed in a solution of pure RhB or adding EDTA-2Na or *t*BuOH.

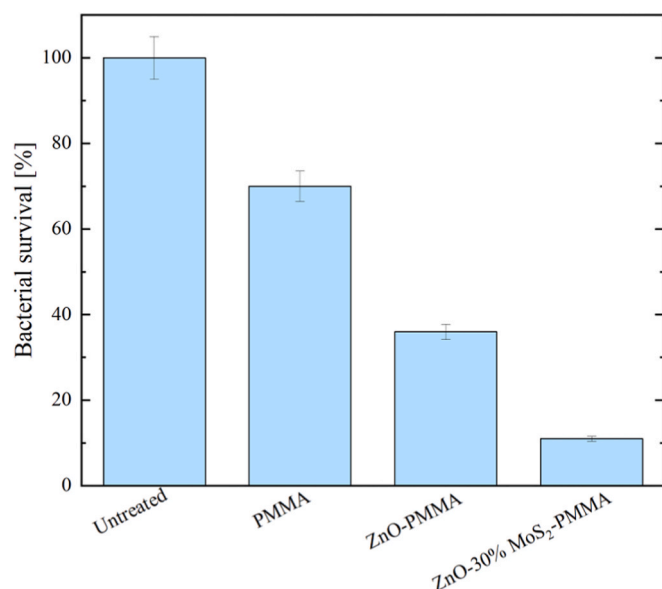| Sample	Rate costant (min^{-1})
ZnO-PMMA (RhB)	$(1.70 \pm 0.09) \times 10^{-3}$
ZnO-PMMA (RhB + t-BuOH)	$(1.44 \pm 0.07) \times 10^{-3}$
ZnO-PMMA (RhB + EDTA)	$(0.70 \pm 0.04) \times 10^{-3}$
ZnO-30 % MoS$_2$-PMMA (RhB)	$(2.64 \pm 0.13) \times 10^{-3}$
ZnO-30 % MoS$_2$-PMMA (RhB + t-BuOH)	$(2.19 \pm 0.11) \times 10^{-3}$
ZnO-30 % MoS$_2$-PMMA (RhB + EDTA)	$(0.78 \pm 0.04) \times 10^{-3}$

Fig. 10. Bacterial survival after 1 h exposure to nanocomposites. Results were normalized toward the untreated sample and reported as percentages.

the heterojunction between ZnO and MoS_2, also stems in an improved antibacterial activity.

Considering all the obtained results we can state, without any doubt, that the increment in the photocatalytic and antibacterial aptitude in the presence of MoS_2 nanoflakes is due to the formation of a heterojunction between ZnO and MoS_2. The intimate contact between the two nanomaterials was indeed testified by the TEM analyses (see Fig. 4). It is important to underline that the contact between the ZnO and MoS_2 nanomaterials, responsible of the formation of the heterojunction, was obtained by simply blending the two materials with the method of sonication, without the need to involve any chemical reactions or long and complicated procedures. No variations in the wettability and, as a consequence, in the adsorption properties of the nanocomposites were observed through the contact angle measurements (see Table 1). The role of MoS_2 in the investigated samples is as a valid co-catalyst. This was verified by PL measurements (see Fig. 5), which indicated a promotion of the photo-generated electrons-holes separation in the presence of MoS_2 nanoflakes. The above discussed outcomes together with the absence of activity under visible light, and the energy level diagrams depicted in the literature [22,23,25] allow to outline the following mechanism: when the ZnO–MoS_2-PMMA composite is irradiated by UV light, the photo-generated holes are transferred from the valence band of ZnO to the valence band of MoS_2, leaving the photo-exited electrons in the conduction band of ZnO. In this way, the electron-hole recombination is reduced and the holes are highly available for the photocatalytic process.

After a careful analysis of the works present in the literature, we found only one work [47] on a similar material realized by coupling TiO_2, MoS_2, and PMMA for photocatalytic applications. A comparison between ref. [47] and the present work evidenced a more simple, rapid and low-cost realization procedure in the present case. Made a comparison between the photocatalytic aptitudes of our composites with respect to the material described by Li et al. [47] is difficult, due to the different materials (ZnO in the present work, TiO_2 in ref. [47]), different experimental conditions (such as the power lamp used, the organic contaminants, etc.), and different surface to volume ratio of the used materials. In any case, it is worth noting that Li and co-workers [47] studied a material in the form of powders, which requires the removal of the photocatalyst after the water treatment. On the contrary, we presented here nanomaterials well anchored to the polymers, more suitable for large scale application.

Even if the nanomaterials resulted anchored to the PMMA matrix, we investigated the eventual toxic of the studied materials through the microcrustacean *Artemia salina*. *Artemia*-based assays are a key tool for toxicology because of the rapidity, low cost and easy to carry out. In addition, there is a tendency to use *Artemia salina* assay in toxicological tests to screen different types of nanoparticles and nanomaterials in order to provide more information on their acute toxicity [37].

As regard the % dead nauplii, it was observed that at 24 h of exposure they were: 3 % for control and ZnO-30 % MoS_2-PMMA group, 6 % for ZnO-PMMA group. At 48 h the percentage of deaths for all groups remained unchanged. No alterations in growth were observed, since all nauplii eye and well-organized appendices: moreover at 48 h for the exposed groups as well as for the control group, no morphological alterations on mandibles and gut were observed as shown in Fig. 11. Nauplii use mandibles to filter water therefore small food particles can be uptake into the gut [48]. Although several studies have shown that nanoparticles and microplastics pollution can damage gut and life cycle of nauplii [37,49], our results pointed out the nontoxicity of the nanomaterials tested on *Artemia salina* nauplii.

4. Conclusions

The ZnO–MoS_2-PMMA composites realized in this work, by the simple method of sonication and solution casting, combine several factors carrying out to the realization of materials potentially useable for photocatalytic applications on a large scale. Thanks to the created heterojunction between ZnO and MoS_2, the polymeric nanocomposites showed a significant photocatalytic efficiency towards the degradation of RhB and SDS (with an increase higher than 50 %, with respect to the materials without MoS_2). The antibacterial properties, tested through *E. coli*, were considerable, too (with an increase of 25 % of dead bacteria with respect to the materials without MoS_2). In addition, the realization of the nanocomposites with PMMA as supporting matrix prevent the dispersion of nanomaterials into the environment overcoming one of their main limits. The eco-safety of the nanocomposites was demonstrated by tests on *Artemia salina*. In conclusion, the nanocomposites here presented offer an innovative and promising alternative to the conventional materials for photocatalytic applications, such as for water treatment.

CRediT authorship contribution statement

Maria Cantarella: Data curation, Investigation, Writing – review & editing. **Vanessa Spanò:** Data curation, Investigation. **Massimo Zimbone:** Data curation, Investigation. **Federico Giuffrida:** Investigation. **Ernestino Lufrano:** Data curation, Investigation. **Vincenzina Strano:** Investigation. **Giorgia Franzò:** Data curation, Investigation. **Gianfranco Sfuncia:** Data curation, Investigation. **Giuseppe Nicotra:** Data curation, Investigation. **Alessandra Alberti:** Data curation, Investigation. **Maria Antonietta Buccheri:** Data curation, Investigation. **Giancarlo Rappazzo:** Investigation. **Elena Maria Scalisi:** Data curation, Investigation. **Roberta Pecoraro:** Data curation, Investigation. **Maria Violetta Brundo:** Data curation. **Giuliana Impellizzeri:** Conceptualization, Funding acquisition, Methodology, Writing – original draft.

Fig. 11. *Artemia salina* larvae at 48 h: (a) nauplio unexposed, (b) nauplio exposed to ZnO-PMMA sample, (c) nauplio exposed to ZnO-30 % MoS$_2$-PMMA sample (10 × magnification).

Declaration of competing interest

The authors declare that they have no known competing financial interests or personal relationships that could have appeared to influence the work reported in this paper.

Data availability

Data will be made available on request.

References

[1] J. Singh, P. Yadav, A.K. Pal, V. Mishra, Water pollutants: Origin and Status, in: D. Pooja, P. Kumar, P. Singh, S. Patil (Eds.), Sensors in Water Pollutants Monitoring Role of Material. Advanced Functional Materials and Sensors, Springer, Singapore, 2020, https://doi.org/10.1007/978-981-15-0671-0_2.

[2] J. Theerthagiri, J. Park, H.T. Das, N. Rahamathulla, E.S.F. Cardoso, A.P. Murthy, G. Maia, D.N. Vo, M.Y. Choi, Electrocatalytic conversion of nitrate waste into ammonia: a review, Environ. Chem. Lett. 20 (2022) 2929–2949, https://doi.org/10.1007/s10311-022-01469-y.

[3] Y. Yu, A. Min, H.J. Jung, J. Theerthagiri, S.J. Lee, K.Y. Kwon, M.Y. Choi, Method development and mechanistic study on direct pulsed laser irradiation process for highly effective dichlorination of persistent organic pollutants, Environ. Pollut. 291 (2021) 118158, https://doi.org/10.1016/j.envpol.2021.118158, 1-6.

[4] J. Theerthagiri, K. Karuppasamy, S.J. Lee, R. Shwetharani, H.S. Kim, S.K.K. Pasha, M. Ashokkumar, M.Y. Choi, Fundamentals and comprehensive insights on pulsed laser synthesis of advanced materials for diverse photo- and electrocatalytic applications, Light Sci. Appl. 11 (2022) 250 1–25047, https://doi.org/10.1038/s41377-022-00904-7.

[5] J. Theerthagiri, S.J. Lee, K. Karuppasamy, S. Arulmani, S. Veeralakshmi, M. Ashokkumar, M.Y. Choi, Application of advanced materials in sonophotocatalytic processes for the remediation of environmental pollutants, J. Hazard Mater. 412 (2021), https://doi.org/10.1016/j.jhazmat.2021.125245, 125245 1-12524519.

[6] S.S. Naik, S.J. Lee, J. Theerthagiri, Y. Yu, M.Y. Choi, Rapid and highly selective electrochemical sensor based on ZnS/Au-decorated f-multi-walled carbon nanotube nanocomposites produced via pulsed laser technique for detection of toxic nitro compounds, J. Hazard Mater. 418 (2021), https://doi.org/10.1016/j.jhazmat.2021.126269, 126269 1-12626913.

[7] M.P. Rayaroth, C.T. Aravindakumar, N.S. Shah, G. Boczkaj, Advanced oxidation processes (AOPs) based wastewater treatment – a serious environmental issue: a review, Chem. Eng. J. 430 (2022), https://doi.org/10.1016/j.cej.2021.133002, 133002 1-13300215.

[8] U.I. Gaya, A.H. Abdullah, Heterogeneous photocatalytic degradation of organic contaminants over titanium dioxide: a review of fundamentals, progress and problems, J. Photochem. Photobiol., A 9 (2008) 1–12, https://doi.org/10.1016/j.jphotochemrev.2007.12.003.

[9] M.N. Chong, B. Jin, C.W.K. Chow, C. Saint, Recent developments in photocatalytic water treatment technology: a review, Water Res. 44 (2010) 2997–3027, https://doi.org/10.1016/j.watres.2010.02.039.

[10] K.M. Lee, C.W. Lai, K.S. Ngai, J.C. Juan, Recent developments of zinc oxide based photocatalyst in water treatment technology: a review, Water Res. 88 (2016) 428–448, https://doi.org/10.1016/j.watres.2015.09.045.

[11] A. Di Mauro, M.E. Fragalà, V. Privitera, G. Impellizzeri, ZnO for application in photocatalysis: from thin films to nanostructures, Mater. Sci. Semicond. Process. 69 (2017) 44–51, https://doi.org/10.1016/j.mssp.2017.03.029.

[12] X.H. Tai, C.W. Lai, J.C. Juan, K.M. Lee, Chapter 8 – Nano-photocatalyst in photocatalytic oxidation processes, in: Nanomaterials for Air Remediation, Elsevier, 2020, https://doi.org/10.1016/B978-0-12-818821-7.00008-7.

[13] M.B. Tahir, M. Nawaz, G. Nabi, M. Sagir, M.I. Khan, N. Malik, Role of nanophotocatalysts for the treatment of hazardous organic and inorganic pollutants in wastewater, Int. J. Environ. Anal. Chem. 102 (2022) 491–515, https://doi.org/10.1080/03067319.2020.1723570.

[14] S.K. Sharma, R. Gupta, G. Sharma, K. Vemula, A.R. Koirala, N.K. Kaushik, E. H. Choi, D.Y. Kim, L.P. Purohit, B.P. Singh, Photocatalytic performance of yttrium-doped CNT-ZnO nanoflowers synthesized from hydrothermal method, Mater. Today Chem. 20 (2021), https://doi.org/10.1016/j.mtchem.2021.100452, 100452 1-10045210.

[15] S. Gayathri, P. Jayabal, M. Kottaisamy, V. Ramakrishnan, Synthesis of ZnO decorated graphene nanocomposite for enhanced photocatalytic properties, J. Appl. Phys. 115 (2014), https://doi.org/10.1063/1.4874877, 173504 1-9.

[16] C. Chen, W. Yu, T. Liu, S. Cao, Y. Tsang, Graphene oxide/WS$_2$/Mg-doped ZnO nanocomposites for solar-light catalytic and anti-bacterial applications, Sol. Energy Mater. Sol. Cells 160 (2017) 43–53, https://doi.org/10.1016/j.solmat.2016.10.020.

[17] C. Han, M.Q. Yang, B. Weng, Y.J. Xu, Improving the photocatalytic activity and anti-photocorrosion of semiconductor ZnO by coupling with versatile carbon, Phys. Chem. Chem. Phys. 16 (2014) 16891–16903, 16891.10.1039/c4cp02189d.

[18] A. Di Mauro, C. Farrugia, S. Abela, P. Refalo, M. Grech, L. Falqui, G. Nicotra, G. Sfuncia, A.M. Mio, M.A. Buccheri, G. Rappazzo, M.V. Brundo, E.M. Scalisi, R. Pecoraro, C. Iaria, V. Privitera, G. Impellizzeri, Novel Ag/ZnO/PMMA nanocomposites for an efficient water reuse, ACS Appl. Bio Mater. 3 (2020) 4417–4426, https://doi.org/10.1021/acsabm.0c00409.

[19] A. Di Mauro, M. Zimbone, M.E. Fragalà, G. Impellizzeri, Effect of Pt nanoparticles on the photocatalytic activity of ZnO nanofibers, Nanoscale Res. Lett. 10 (2015) 484, https://doi.org/10.1186/s11671-015-1126-6, 1-7.

[20] K.F. Mak, C. Lee, J. Hone, J. Shan, T.F. Heinz, Atomically thin MoS$_2$: a new direct-gap semiconductor, Phys. Rev. Lett. 105 (2010), https://doi.org/10.1103/PhysRevLett.105.136805, 136805 1-4.

[21] B. Qu, Q. Ouyang, X. Yu, W. Luo, L. Qi, Y. Chen, Nonlinear absorption, nonlinear scattering, and optical limiting properties of MoS$_2$-ZnO composite-based organic glasses, Phys. Chem. Chem. Phys. 17 (2015) 6036–6043, https://doi.org/10.1039/c4cp05227g.

[22] G.P. Awasthi, S.P. Adhikari, S. Ko, H.J. Kim, C.H. Park, C.S. Kim, Facile synthesis of ZnO flowers modified graphene like MoS$_2$ sheets for enhanced visible-light-driven photocatalytic activity and antibacterial properties, J. Alloys Compd. 682 (2016) 208–215, https://doi.org/10.1016/j.jallcom.2016.04.267.

[23] Y.C. Chang, Y.W. Lin, M.Y. Lu, Construction of MoS$_2$/ZnO heterostructures as highly efficient photocatalysts for enhanced visible-light decomposition of methylene blue and hydrogen evolution, Mater. Chem. Phys. 266 (2021), https://doi.org/10.1016/j.matchemphys.2021.124560, 124560 1-7.

[24] R.A. Geioushy, I.M. Hegazy, S.M. El-Sheikh, O.A. Fouad, Construction of 2D MoS$_2$@ZnO heterojunction as superior photocatalyst for highly efficient and selective CO$_2$ conversion into liquid fuel, J. Environ. Chem. Eng. 10 (2022), https://doi.org/10.1016/j.jece.2022.107337, 107337 1-10733710.

[25] Y. Fu, Z. Ren, J. Wu, Y. Li, W. Liu, P. Li, L. Xing, J. Ma, H. Wang, X. Xue, Direct Z-scheme heterojunction of ZnO/MoS$_2$ nanoarrays realized by flowing-induced piezoelectric field for enhanced sunlight photocatalytic performances, Appl. Catal. B Environ. 285 (2021), https://doi.org/10.1016/j.apcatb.2020.119785, 119785 1-11978510.

[26] J. Pan, P. Wang, Z. Chen, Q. Yu, P. wang, M. Zhu, W. Zhao, J. Wang, Y. Zheng, C. Li, The Pt-free 1T/2H-MoS$_2$/CdS/MnO$_x$ hollow core-shell nanocomposites toward overall water splitting via HER/OER synergy of 1T-MoS$_2$/MnO$_x$, Mater. Today Chem. 21 (2021), https://doi.org/10.1016/j.mtchem.2021.100528, 100528 1-10052810.

[27] E. Kabir, V. Kumar, K.H. Kim, A.C.K. Yip, J.R. Sohn, Environmental impacts of nanomaterials, J. Environ. Manag. 225 (2018) 261–271, https://doi.org/10.1016/j.jenvman.2018.07.087.

[28] X. Zhao, L. Lv, B. Pan, W. Zhang, S. Zhang, Q. Zhang, Polymer-supported nanocomposites for environmental application: a review, Chem. Eng. J. 170 (2011) 381–394, https://doi.org/10.1016/j.cej.2011.02.071.

[29] M. Cantarella, G. Impellizzeri, A. Di Mauro, V. Privitera, S.C. Carroccio, Innovative polymeric hybrid nanocomposites for application in photocatalysis, Polymers 13 (2021) 1184 1–118422, https://doi.org/10.3390/polym13081184.

[30] A. Di Mauro, M. Cantarella, G. Nicotra, G. Pellegrino, A. Gulino, M. V Brundo, V. Privitera, G. Impellizzeri, Novel synthesis of ZnO/PMMA nanocomposites for photocatalytic applications, Sci. Rep. 7 (2017) 40895 1–4089512, https://doi.org/10.1038/srep40895.

[31] M. Ussia, A. Di Mauro, T. Mecca, F. Cunsolo, G. Nicotra, C. Spinella, P. Cerruti, G. Impellizzeri, V. Privitera, S.C. Carroccio, ZnO-pHEMA nanocomposites: an ecofriendly and reusable materials for water remediation, ACS Appl. Mater. Interfaces 10 (2018) 40100–40110, https://doi.org/10.1021/acsami.8b13029.

[32] M. Cantarella, R. Sanz, M.A. Buccheri, F. Ruffino, G. Rappazzo, S. Scalese, G. Impellizzeri, L. Romano, V. Privitera, Immobilization of nanomaterials in PMMA composites for photocatalytic removal of dyes, phenols and bacteria from water, J. Photochem. Photobiol., A 321 (2016) 1–11, https://doi.org/10.1016/j.jphotochem.2016.01.020.

[33] N.N. Hafizah, M.H. Mamat, C.M.S. Said, M.H. Abidin, M. Rusop, Thermal degradation of nanocomposited PMMA/TiO₂ nanocomposites, IOP Conf. Ser. Mater. Sci. Eng. 46 (2013), https://doi.org/10.1088/1757-899X/46/1/012045, 012045 1-8.

[34] H. Zhang, R. Zong, Y. Zhu, Photocorrosion inhibition and photoactivity enhancement for zinc oxide via hybridization with monolayer polyaniline, J. Phys. Chem. C 113 (2009) 4605–4611, https://doi.org/10.1021/jp810748u.

[35] C. Minero, G. Mariella, V. Maurino, D. Vione, E. Pelizzetti, Photocatalytic transformation of organic compounds in the presence of inorganic ions. 2. Competitive reactions of phenol and alcohols on a titanium dioxide-fluoride system, Langmuir 16 (2000) 8964–8972, https://doi.org/10.1021/la0005863.

[36] ISO 27447, Fine Ceramics (Advanced Ceramics, Advanced Technical Ceramics) - Test Method for Antibacterial Activity of Semiconducting Photocatalytic, 2019.

[37] R. Pecoraro, E.M. Scalisi, G. Messina, G. Fragalà, S. Ignoto, A. Salvaggio, M. Zimbone, G. Impellizzeri, M.V. Brundo, *Artemia salina*: a microcrustacean to assess engineered nanoparticles toxicity, Microsc. Res. Tech. 84 (3) (2021) 531–536, https://doi.org/10.1002/jemt.23609.

[38] P. Manzini, R. Azzoni, G. Sansoni, R. Spaggiari, G.N. Baldaccini, R. Fochetti, L. Mancini, Saggio di tossicità acuta con *Artemia sp.* (Metodi per la determinazione di effetti tossici acuti con *Artemia sp.*), Bollettino CISBA n 1 (1997).

[39] Y. Yuan, T.R. Lee, Contact angle and wetting properties, in: G. Bracco, B. Holst (Eds.), Surface Science Techniques, Springer Series in Surface Sciences, vol. 51, Springer, Berlin, Heidelberg, 2013, https://doi.org/10.1007/978-3-642-34243-1_1.

[40] P. Makuła, M. Pacia, W. Macyk, How to correctly determine the band gap energy of modified semiconductor photocatalysts based on UV-Vis spectra, J. Phys. Chem. Lett. 9 (23) (2018) 6814–6817, https://doi.org/10.1021/acs.jpclett.8b02892.

[41] Ü. Özgür, Y.I. Alivov, C. Liu, A. Teke, M.A. Reshchikov, S. Doan, V. Avrutin, S. J. Cho, H, Morkoc¸ A comprehensive review of ZnO materials and devices, J. Appl. Phys. 98 (2005) 1–304, https://doi.org/10.1063/1.1992666.

[42] D.J. Lee, H.M. Kim, J.Y. Kwon, H. Choi, S.H. Kim, K.B. Kim, Structural and electrical properties of atomic layer deposited Al-doped ZnO films, Adv. Funct. Mater. 21 (2011) 448–455, https://doi.org/10.1002/adfm.201001342.

[43] I. Udom, M.K. Ram, E.K. Stefanakos, A.F. Hepp, D.Y. Goswami, One dimensional-ZnO nanostructures: synthesis, properties and environmental applications, Mater. Sci. Semicond. Process. 16 (2013) 2070–2083, https://doi.org/10.1016/j.mssp.2013.06.017.

[44] M.Y. Lei, C.M. Liu, Y.G. Zhou, Z.H. Yan, S.B. Han, W. Liu, X. Xiang, X.T. Zu, Microstructure and photoluminescence of MoS₂ decorated ZnO nanorods, Chin. J. Phys. 54 (2016) 51–59, https://doi.org/10.1016/j.cjph.2016.03.003.

[45] H.M. Nguyen, C.M. Phan, T. Sen, Degradation of sodium dodecyl sulfate by photoelectrochemical and electrochemical processes, Chem. Eng. J. 287 (2016) 633–639, https://doi.org/10.1016/j.cej.2015.11.074.

[46] N. Singh, G. Jabbour, U. Schwingenschlogl, Optical and photocatalytic properties of two-dimensional MoS₂, Eur. Phys. J. B 85 (2012) 392 1–4, https://doi.org/10.1140/epjb/e2012-30449-7.

[47] Y. Li, Z. Wang, H. Zhao, X. Huang, M. Yang, 3D MoS₂@TiO₂@poly(methyl methacrylate) nanocomposite with enhanced photocatalytic activity, J. Colloid Interface Sci. 557 (2019) 709–721, https://doi.org/10.1016/j.jcis.2019.09.074.

[48] M. Ates, J. Daniels, Z. Arslan, I.O. Farah, H.F. Rivera, Comparative evaluation of impact of Zn and ZnO nanoparticles on brine shrimp (Artemia salina) larvae: effects of particle size and solubility on toxicity, Environ. Sci. Process Impacts 15 (2013) 225–233, https://doi.org/10.1039/c2em30540b.

[49] M. Albano, G. Panarello, D. Di Paola, F. Capparucci, R. Crupi, E. Gugliandolo, N. Spanò, G. Capillo, S. Savoca, The influence of polystyrene microspheres abundance on development and feeding behavior of Artemia salina (Linnaeus, 1758), Appl. Sci. 11 (8) (2021) 3352 1–335217, https://doi.org/10.3390/app11083352.